THE ASTROPHYSICAL JOURNAL, 405:337–352, 1993 March 1

FORMATION OF THE CIRCUMSTELLAR SHELL AROUND SN 1987A

JOHN M. BLONDIN[1]
Department of Physics and Astronomy, University of North Carolina, CB 3255, Chapel Hill, NC 27599
AND
PETER LUNDQVIST
Department of Astronomy, University of Virginia, P.O. Box 3218, Charlottesville, VA 22903
Received 1992 June 18; accepted 1992 September 8

ABSTRACT

The nebulosity within a few arcseconds from SN 1987A has been modeled in terms of the supernova progenitor's fast wind interacting with a slow, asymmetric, previously emitted red supergiant wind. Previous models have relied on the assumption that the shocked blue supergiant wind is isobaric. We show that this approximation is unsatisfactory, and present two-dimensional time-dependent hydrodynamic calculations of the colliding winds model. From adiabatic models it is found that a ratio of equatorial to polar mass-loss rate during the red supergiant stage of at least ~ 20 is needed to explain the observed structure. It is shown that not only this ratio, but also the form of polar dependence on asymmetry, is important to the formation of a compact ring structure. Models are also presented in which radiative cooling of the shocked red supergiant wind is included and, at early times, also radiative cooling of the shocked blue supergiant wind. Cooling acts to lower the expansion velocity and to increase filamentation. We arrive at a viable colliding winds model for the formation of the circumstellar structure around SN 1987A consisting of a red supergiant wind with a velocity of 5 km s^{-1} and a mass-loss rate of $2 \times 10^{-5}\ M_\odot\ yr^{-1}$, and a blue supergiant wind with a velocity of 300 km s^{-1} and mass-loss rate of $3 \times 10^{-7}\ M_\odot\ yr^{-1}$. This model can explain the low expansion velocity and high density of the ring, as well as the compact ring structure and the morphology of the extended lobes. For the model to be successful, roughly 50% of the red supergiant wind mass is collimated with 10° from the equatorial plane. Such a strong collimation may indicate that the supernova progenitor had a binary companion. Finally, we discuss the implications of the hydrodynamic models in the context of the observed radio emission and high-resolution optical observations.

Subject headings: circumstellar matter — hydrodynamics — stars: individual (SN 1987A) — supernovae: individual (SN 1987A)

1. INTRODUCTION

Observations with the New Technology Telescope (NTT; Wampler et al. 1990), and to higher spatial resolution with the *Hubble Space Telescope* (*HST*; Jakobsen et al. 1991), show that the line emission from the region closest to the supernova (SN) is dominated by an elliptical structure. The minor axis of the ellipse has an observed position angle of 170° ± 5°, and the ratio of major to minor axes is ~1.4. The radial extent of the nebula along its major axis is ~0.″84, corresponding to $\sim 6.3 \times 10^{17}$ cm at a distance of 50 kpc. The gas observed with the *HST* is most likely closely related to the gas emitting the narrow UV lines observed with the *International Ultraviolet Explorer* (*IUE*) a few hundred days after the explosion (Fransson et al. 1989).

Because the *HST* pictures show that the inside of the ellipse is nearly empty of emission (Jakobsen et al. 1991), the observed structure is most likely physical and not just a limb-brightening effect of an elliptical nebula that is complete around the SN. The idea of a ring geometry is supported by the velocity structure of the nebulosity, which gives a larger velocity shear across the ellipse's minor axis than along its major axis (Crotts & Heathcote 1991). If the ellipse is a projection effect of a circular ring tilted by ~43° to the line of sight toward Earth, the observed velocity structure translates into an expansion or contraction velocity of 10.3 km s^{-1}. Further support for a circumstellar ring is provided by models for the UV line light curves (Felten & Dwek 1991; Lundqvist 1991; Luo 1991), which give better fits to the observations for a ring than for a spherical shell (Lundqvist & Fransson 1991).

The NTT observations show that the ring is connected to an outer structure which forms loops with largest extensions (roughly 2.″5) along the ellipse's minor axis. The loops are seen both in lines and in the continuum, indicating that the radiating gas is mixed with dust. On day 735, the integrated emission from the loops in [O III] λ5007 was somewhat less than 10% of the corresponding emission from the ring (E. J. Wampler & L. Wang 1992, private communication). Wampler et al. (1990) note that a bipolar nebula similar to what is seen for many planetary nebulae (PNs) could also explain the observed structure around SN 1987A. In contrast to the ring, the observed loops should be due to limb brightening.

The supernova progenitor, Sk −69°202, was undoubtedly a blue supergiant (BSG) immediately prior to the SN explosion, classified by Rousseau et al. (1978) as B3 Ia. The observed bipolar nebula is most naturally explained by asymmetric mass loss during the star's red supergiant (RSG) stage (Luo & McCray 1991, hereafter LM; Wang & Mazzali 1992, hereafter WM), which according to evolutionary calculations must have preceded the final BSG stage (Arnett 1988; Shigeyama, Nomoto, & Hashimoto 1988; Woosley 1988). The cause of the

[1] Current address: Department of Physics, North Carolina State University, P.O. Box 8202, Raleigh, NC 27695.

asymmetry is not known, but it may be due to a binary companion, as has been proposed for PNs (Morris 1981). As of now, however, there is no direct evidence for a companion, although Chevalier (1992a) and Podsiadlowski (1992) note that explanations for some observed features of the SN could benefit from a binary evolution.

LM and WM modeled the interaction of the BSG wind with the slow RSG wind using the thin-shell approximation. This method assumes that the shocked BSG wind has a uniform pressure throughout the interior of the wind bubble and that the shocked RSG wind forms an infinitesimally thin shell surrounding this bubble. Both groups were able to model the structure of the observed nebula, although they used very different seed asymmetries. While LM prefer a ratio of equatorial to polar mass-loss rate of 5, WM suggested a value of only 1.25. It is not clear why these results differ to this large extent.

An alternative explanation to the ring structure and especially the extended nebulosity was provided by Podsiadlowski, Fabian, & Stevens (1991). They too invoked a binary evolution, but they assume that the observed structure arises as a result of a collision of the winds from the two stars. As noted by Felten & Dwek (1992), this model may have troubles with orientation, and may also be incompatible with recent NTT images (L. Wang & E. J. Wampler 1992, private communication).

Here we assume the same colliding winds scenario as LM and WM, but instead of a simplistic thin-shell, isobaric-interior approximation, we use a full two-dimensional time-dependent hydrodynamical approach. In § 2 we describe the colliding winds model for the formation of the circumstellar ring around SN 1987A. We discuss the numerical methodology used in solving the equations of hydrodynamics in § 3. In § 4 we present the results of our hydrodynamic simulations. In § 5 we discuss the implications of these calculations and suggest an alternative to the standard model used by previous authors. We conclude with a discussion of the results and their application to the circumstellar structure around SN 1987A in § 6, and a brief summary in § 7.

2. COLLIDING WINDS MODEL

The evolution of the progenitor to SN 1987A from a RSG star emitting a slow, dense wind to a BSG star emitting a relatively fast wind is expected to produce a circumstellar shell of wind material as the fast blue wind overtakes and sweeps up the slow red wind. Given this history of the SN 1987A progenitor, it is natural to expect the presence of a circumstellar shell surrounding the SN. Indeed, Chevalier & Fransson (1987) went so far as to predict such a structure. It is not surprising, therefore, that a shell structure has in fact been observed. Rather, it is the asymmetry of the circumstellar shell that has drawn so much attention. By reason of deduction it has been assumed that the asymmetric shell is a result of an asymmetry in either the RSG wind or the subsequent BSG wind. Within the context of the thin-shell approximation, the asymmetry must reside in the RSG wind because any asymmetry in the BSG wind will be smoothed out inside the region of isobaric shocked BSG wind (LM).

A standard model has thus arisen whereby a fast BSG wind overruns a slow RSG wind with a slightly higher density along the equator than along the symmetry axis. Previous authors have adopted parameters for these stellar winds as suggested by Lundqvist & Fransson (1991) and listed in Table 1. We will discuss the observational constraints on these parameters in § 5.1. In this model the BSG wind sweeps up the RSG wind into a shell, as in the formation of a normal stellar wind bubble. The expansion of the shell is driven by the high thermal pressure of the BSG wind heated in the reverse wind shock formed at a small radius. Because of the higher density in the RSG wind on the equator than along the poles, this stellar wind bubble pushes out faster along the low-density poles, forming the shape of a peanut. The high-density gas of the shocked RSG wind in the "waist" of the peanut-shaped shell is suggested to produce the observed ring seen by *HST*, while limb brightening of the two lobes of the peanut-shaped shell creates the loops seen with the NTT.

TABLE 1

WIND PARAMETERS FOR THE STANDARD MODEL

Parameter	Value
$\dot{M}_b$	$2.0 \times 10^{-6}\ M_\odot\ \mathrm{yr}^{-1}$
$\dot{M}$	$1.0 \times 10^{-5}\ M_\odot\ \mathrm{yr}^{-1}$
v_b	$550\ \mathrm{km\ s}^{-1}$
v_r	$10\ \mathrm{km\ s}^{-1}$

If we neglect for the moment any possible tangential motions in the interior of the wind bubble or in the thin shell, i.e., assume only radial motions are relevant, we find that these standard wind parameters cannot explain the slow expansion velocity of the ring. This was evident early on when Chevalier (1988) predicted an expansion velocity of at least 33 km s^{-1} using rather extreme parameters for the RSG wind. To provide a background with which to understand the expansion rates, let us quickly review the one-dimensional solutions for the expansion velocity in the case of adiabatic winds, a rapidly cooling outer shock, and two isothermal winds (both inner and outer shocks rapidly cooling).

If both winds are spherically symmetric, adiabatic, and have constant mass-loss rates and velocities, the interaction region between the fast wind and the slower outer wind takes on a self-similar form (Chevalier & Imamura 1983). As an example, we consider the strong shock (Mach number $\rightarrow \infty$) case with $\dot{M}_r/\dot{M}_b = 10$ and $v_b/v_r = 55$, appropriate for the assumed wind parameters of the SN 1987A progenitor allowing for a factor of 3 higher mass-loss rate along the equator than the average ($\dot{M}_r = 3 \times 10^{-5}\ M_\odot\ \mathrm{yr}^{-1}$ along the equator). From Figure 5 of Chevalier & Imamura we find a shock velocity ratio of $v_r/s_r \approx 0.15$, where s_r is the propagation velocity of the outer shock into the RSG wind. For $v_r = 10$ km s^{-1} this corresponds to an expansion velocity for the circumstellar ring of 67 km s^{-1}.

If the outer shock is sufficiently slow and the RSG wind is sufficiently dense, then we might expect the gas behind the outer shock to cool rapidly (§ 4.4; LM). In this case Chevalier (1988) wrote down an approximate expansion velocity by assuming that the outer shell is geometrically thin and that the shocked BSG wind is isobaric. With these assumptions, the expansion can be described by the equations of mass and momentum conservation of the thin shell and by energy conservation of the shocked BSG wind. The resulting expression for the expansion velocity v_{exp} is

$$\frac{v_{\mathrm{exp}}}{v_r}\left(\frac{v_{\mathrm{exp}}}{v_r} - 1\right)^2 = \frac{1}{2\alpha + \beta}\,\frac{\dot{M}_b v_b^2}{\dot{M}_r v_r^2}, \qquad (1)$$

where α is the ratio of the pressure immediately behind the thin shell to the average pressure in the shocked BSG wind, and β is

the volume fraction of the shell interior occupied by the shocked BSG wind. From one-dimensional numerical simulations we find that the ratio $1/(2\alpha + \beta)$ is very close to $\frac{1}{3}$ for the wind parameters assumed above. Using these wind parameters, this approximation gives an expansion velocity of 47 km s^{-1}. This is somewhat slower than the adiabatic solution because entropy is being lost from the shocked RSG wind.

If both the inner and the outer shocks are radiatively cooling, one need only balance the ram pressures of the winds to find the expansion velocity:

$$v_{\rm exp} = \frac{v_r + \chi v_b}{1 + \chi}, \quad \text{where} \quad \chi = \left(\frac{\dot{M}_b v_r}{\dot{M}_r v_b}\right)^{1/2}. \tag{2}$$

For the above parameters this solution gives an expansion velocity of 32 km s^{-1}. Again, this solution is slower than the previous two because of the loss of entropy and hence lack of thermal pressure to drive the expansion. All three of these expansion velocities are much higher than the observed 10.3 km s^{-1}, suggesting either radically different wind parameters or significant nonradial motion.

In the presence of non-radial motions a slower ring expansion velocity may be possible. In effect these motions must either decrease the momentum transfer to the ring, e.g., by decreasing the pressure driving the ring expansion, or increase the inertia of the ring, e.g., through a converging mass flow onto the equator. The thin-shell model of LM produced an expansion velocity of the ring at the current epoch of only 16 km s^{-1} as a result of a convergence of swept-up mass onto the equator. However, this result is strongly dependent on the formation of a tight cusp on the equator to provide the oblique shocks needed to redirect flow to the equator. As we shall see below, we do not expect such a cusp to form. In order to model the evolution of the asymmetric shell in this standard model more accurately, we have applied the modern tools of computational hydrodynamics and supercomputers.

3. NUMERICAL METHOD

We have employed two-dimensional time-dependent hydrodynamic computations to investigate the evolution of the interaction region between the RSG wind and the subsequent BSG wind in the above-described model for the progenitor of SN 1987A. Previous work on the circumstellar structure of SN 1987A has relied upon the Kompaneets approximation to simplify the evolution of the wind interaction. This approximation is valid only in the limit of the sound speed in the shocked inner wind being much greater than the expansion speed of the interaction region. For the standard model discussed in the literature this is only marginally valid, and time-dependent hydrodynamic calculations are necessary to study the evolution of the winds.

We have used the hydrodynamics code VH-1 in the computations presented below. This code is based on the piecewise parabolic method (PPM) developed by Colella & Woodward (1984), and is formulated as a Lagrangian (fluid-frame) calculation followed by a remap of the conserved quantities onto the original Eulerian grid. The high spatial accuracy of this code provides significantly better resolution than other methods on comparable grids. A critical comparison of PPM and other numerical methods can be found in Woodward & Colella (1984).

The calculations presented here are run in spherical coordinates with reflecting boundary conditions at the equator and pole. The grid is expanded in the radial direction to track the forward shock (usually along the symmetry axis), and the inner and outer boundaries are set to input the blue and red winds, respectively. This grid expansion is critical for following the evolution to the late times associated with the current epoch of the ring/shell around SN 1987A. A small amount of dissipation is required to reduce the postshock noise present in this code when strong shocks move very slowly with respect to the computational grid (a direct result of tracking the forward shock). We have accomplished this by wiggling the grid back and forth in the angular direction a fraction of a zone each time step (see Colella & Woodward 1984). Most of the simulations discussed here were run on a grid of 200 × 200 zones with the radius spanning a factor of 20. VH-1 runs at a speed of approximately 60,000 zones per CPU second on the Cray YMP, resulting in run times of ~1 hr for a typical simulation of 5000 time steps. For reasons discussed in § 4.4 we have assumed that both winds are adiabatic in all but a few of the simulations. Simulations including radiative cooling are presented in §§ 4.4 and 5.3.

4. RESULTS

The numerical code was first tested on the one-dimensional problem of spherically symmetric interacting winds. For strictly adiabatic winds we can use the solutions of Chevalier & Imamura (1983) to test the hydrodynamics code. To minimize the error from reading values off Figure 5 of their paper, we have chosen shock velocity ratios $b_r \equiv v_r/s_r = 0.2$ and $b_b \equiv v_b/s_b = 10$, where s_r (s_b) is the propagation velocity of the outer (inner) wind shock. From their Figure 5 we find that these shock ratios correspond to wind parameters of $\dot{M}_r/\dot{M}_b = 5.0$ and $v_b/v_r = 25.9$. Using these wind ratios, our hydrodynamics code reached a value of $b_r = 0.2$ after expanding a factor of 10 in radius. When radiative cooling is included, we do not expect such accurate results, owing to the poor resolution of the cooling region behind the shock. We were nonetheless able to reproduce the expansion velocity given by equation (1) to within a few percent (see § 4.4). To approximate the interaction of isothermal winds as described by equation (2), we ran a one-dimensional simulation with $\gamma = 1.01$. The expansion velocity in this simulation was 33 km s^{-1} for the wind parameters used in § 2, slightly larger than the value obtained with equation (2). The difference may be attributed to the fact that the simulation was not exactly isothermal, and hence there was a slightly larger pressure in the shocked BSG wind to drive the expansion faster.

The two-dimensional simulations are evolved on an expanding grid so that the interaction region between the winds can be tracked for several expansion times. The grid is initialized with the two winds separated by a spherical shock at a radius of 2×10^{15} cm and allowed to evolve to the point where the equatorial ring is at a radius of $R_{\rm eq} \approx 6.3 \times 10^{17}$ cm (see § 1). We will use the results of our standard model to illustrate the evolution of the interaction region in the next subsection. In the remainder of this section we will address the effects of different density ratios in the RSG wind, different asymmetry functions in the wind, and the role of radiative cooling behind the leading shock.

4.1. *Standard Model*

Our standard model follows that of the previous authors, using the wind parameters shown in Table 1. For reference, the self-similar solutions of Chevalier & Imamura (1983) give an

expansion velocity for such winds in spherical symmetry of ~ 78 km s^{-1}. We assume a polar angle dependence in the mass-loss rate of the RSG wind of the form

$$\dot{M}_r(\theta) = \frac{3\dot{M}_r}{3 - A}(1 - A\cos^2\theta)\,. \quad (3)$$

This is the same function as used in LM, and of the same form as that used by WM, but normalized to give the same total mass-loss rate independent of the value of A. [The normalization used in LM is off by a factor of $(3a + 1)/(3a - 1) \approx 1.57$ for $a = 1.5$.] For our standard model we assume a value of $A = 0.8$, corresponding to a density ratio of 5 between the equator and pole (as in LM).

Figure 1 shows the density structure of the interacting winds at four epochs, illustrating the evolution of the interaction region from the initial spherical shape through the time-dependent hourglass phase. As the evolution begins, the characteristic two-shock structure is quickly established, with the inner shock driving back to roughly half the radius of the outer shock (Fig. 1*a*). The width of the shell of shocked RSG wind is less than 10% of the shell radius. As a consequence, the contact discontinuity separating the shocked blue wind from the shocked red wind conforms closely to the outer shock. The outer shock soon begins to deviate from spherical symmetry owing to the anisotropic RSG wind. After one expansion time, R/s_r (Fig. 1*b*), the shell structure appears very similar to the hydrodynamic simulations of Icke, Balick, & Frank (1992) for small values of their parameter β. The inner wind shock is slightly aspherical, and the outer shock surface forms the shape of a peanut. The contact surface is dragged upward at the point where the outer shock forms a cusp. This feature is visible in many of the models presented in Icke et al. (1992). After approximately two expansion times (Fig. 1*c*) the shell structure settles into a roughly static shape, maintaining a self-similar expansion from this point on.

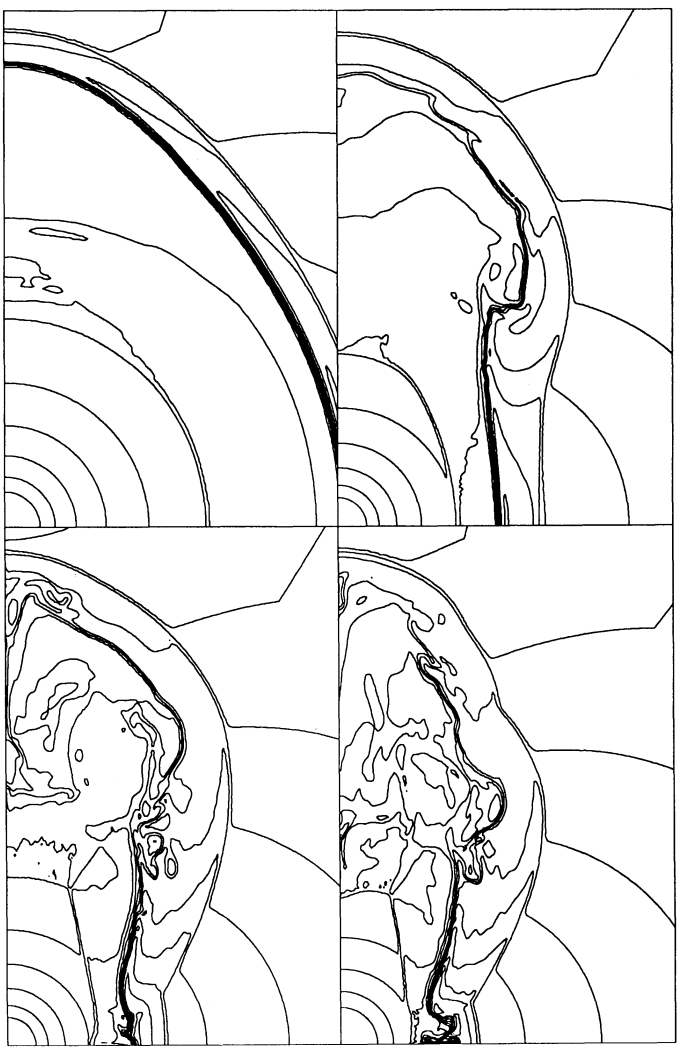

FIG. 1.—Evolution of an adiabatic stellar wind bubble for parameters appropriate to the standard model (model b). The contour lines mark the isodensity surface in increments of 2. The radii of the outer shock at the equator and the corresponding ages for each image are 1.67×10^8 s, 2.81×10^{15} cm (*top left*), 1.90×10^9 s, 1.37×10^{16} cm (*top right*), 1.56×10^{10} s, 9.58×10^{16} cm (*bottom left*), and 1.04×10^{11} s, 6.20×10^{17} cm (*bottom right*).

Within one expansion time in the evolution of the winds two important effects come into play that are not accounted for in the thin-shell models: the asymmetry of the inner shock, and shear instabilities along the contact discontinuity. As the shell of shocked RSG wind begins to creep inward along the equator (in the comoving frame), it begins to squeeze in on the inner wind shock. In the Kompaneets approximation the short sound crossing time would ensure that the pressure behind the inner shock at the equator is the same as at the pole, and the shock would remain spherical. In our simulation the sound speed is not fast enough to equilibrate the pressures, with the result that the inner shock is pushed to a smaller radius on the equator than on the pole.

The ram pressure of the blue wind at the inner shock falls off with the inverse square of the radius owing to the decrease in the density of the wind. The immediate postshock pressure is thus larger behind the inner shock where it is formed at smaller radii. The inner shock asymmetry thus leads to a high-pressure region near the equator (Fig. 2). This overpressure drives a strong flow from the equator up into the lobe. This flow is enhanced by the oblique inner shock around an angle of $\pi/4$, which bends the wind upward along the pole. This directed flow contributes substantial ram pressure in the direction of the pole, leading to an expansion velocity of the lobe larger than predicted by simple models. This enhanced expansion contributes to the pressure gradients driving the interior flow by decreasing the thermal pressure in the lobes due to adiabatic expansion. This may explain why the isobaric approximation is so poor even for an interior sound speed several times larger than the expansion velocity: a small pressure gradient leads to a ram-pressure contribution that expands the lobes, increasing the pressure gradient and thereby increasing the ram-pressure component. At late times the shape of the inner shock resembles that of a rectangle. This large asymmetry leads to supersonic motion within the shocked BSG wind, and additional weak shocks are seen to form occasionally in this region. In Figure 2 the flow speeds in the shocked BSG wind approach a Mach number of 5. The shape of the inner shock is continually changing throughout the late-time evolution, ranging anywhere from a sphere to a cylinder with aspect ratio up to 3:1.

The upward flow from the equator moves along the inner edge of the contact discontinuity from the equator to the pole, creating a shear layer that is subject to the familiar Kelvin-Helmholtz instability. Subsequent evolution shows a continued rippling of the inner surface of the shell of shocked RSG

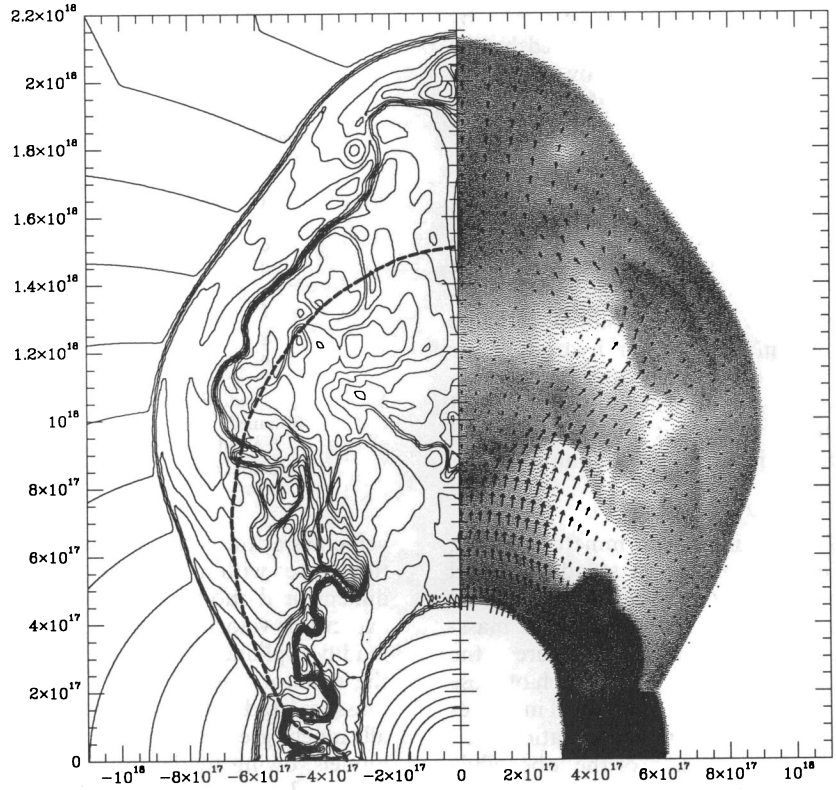

FIG. 2.—Structure of the stellar wind bubble in the adiabatic standard model. The right half of the figure is a halftone image of the gas pressure, with the scale spanning a range of 300. These large pressure gradients drive an outflow in the general direction of the polar lobe. Velocity vectors are plotted for the interior of the stellar wind bubble (but not the unshocked BSG wind). The largest velocity vector corresponds to a velocity of 550 km s^{-1}. The left half is a contour plot of the density with the contour lines spaced at logarithmic invervals of $2^{1/2}$. The heavy dashed line is the shape of the circumstellar shell derived using the Kompaneets approximation.

wind due to this instability. Occasionally clumps of the shell matter are pulled away and advected up into the lobe.

The flow pattern within the wind bubble is dominated by a transonic upward flow leading into a large vortex. When the upward flow reaches the shell it is partially deflected toward the symmetry axis by the expanding shell. Because of the imposed symmetry the flow cannot cross this boundary and is forced downward. This downward flow produces a density enhancement along the symmetry axis that can be seen in many of our simulations. Eventually this downward flow along the axis meets the high-pressure region behind the inner shock and is pushed back out into the lobe. The resulting flow pattern forms a large vortex (a vortex ring in three dimensions) within the shocked blue wind region. This flow pattern is not necessarily expected in unrestricted three-dimensional geometry. Rather, we might expect several competing vortices at several azimuthal angles, all coming together in the vicinity of the polar axis. The competition of these vortices might then give rise to nonaxisymmetric structure in the extended lobes of the stellar wind bubble.

The structure of the interaction region is very different from that suggested by the Kompaneets approximation of isobaric shocked blue wind. Using the self-similar solutions of Chevalier & Imamura (1983), we find a sound speed in the shocked BSG wind of $c_s \approx 300$ km s^{-1}, giving a ratio of sound speed to expansion velocity of roughly 2.8. While this is indeed greater than unity, it does not sufficiently satisfy the criterion that $c_s \gg s_1$. In Figure 2 we have plotted a halftone image of the gas pressure to show the strong pressure variations within the shocked BSG wind, and hence the inaccuracy of an isobaric approximation. The pressure variations span a factor of over 300 in the interior of the wind bubble. The highest pressure region is found on the equator, where the local pressure is a factor of 20 higher than the average interior pressure.

Also shown in Figure 2 is the location of the outer shock as given by the Kompaneets approximation used in previous work. While this approximation assumes an isothermal outer shock, our numerical simulations suggest that the overall shape of the outer shock is not significantly different if the outer shock is adiabatic or isothermal (see § 4.4). The two primary differences between our simulations and the thin-shell models are the larger extent of the shell along the poles and the absence of a cusp at the equator. The enhanced expansion of the lobes is attributed to the strong pressure variations of the bubble interior. As described above, the high equatorial pressure drives a flow into the interior, producing a significant ram pressure on the inside of the shell at the polar lobes. This additional ram pressure increases the expansion rate of the lobes over the thermal-pressure–driven estimate. In the Kompaneets model the lobe expansion is close to the one-dimensional analytic result (eq. [1]), with an expansion velocity of 97 km s^{-1}. In the adiabatic simulation the lobes are expanding with a much higher velocity (222 km s^{-1}) than predicted by the one-dimensional adiabatic estimate (116 km s^{-1}).

The absence of a cusp is also due to the high-pressure region formed at the equator, a feature which is not accounted for in the isobaric approximation of the Kompaneets model. This

high equatorial pressure prevents the formation of a cusp by pushing the shell at the equator faster than predicted by the Kompaneets model. This difference is amplified by the role of the oblique shocks in the Kompaneets model. LM attribute the low equatorial expansion velocity in the Kompaneets model to the converging effect of the oblique shocks in the cusp. These oblique shocks focus the RSG wind onto the equator, increasing the mass in the ring and hence slowing the expansion for a given interior pressure. The combination of increased mass in the ring and decreased pressure driving the expansion of the ring leads to a ring velocity of only ~ 16 km s^{-1} in the Kompaneets model compared with the one-dimensional estimate given by equation (1) of 59 km s^{-1}. In our hydrodynamic models the high equatorial pressure prevents any cusp formation, and thus no oblique shocks are present to focus the RSG wind. As a result, the expansion velocity at the equator is well approximated by the one-dimensional adiabatic solution.

TABLE 2

EXPANSION VELOCITIES (km s^{-1})

			RING		LOBE	
MODEL	ρ_e/ρ_p	β	1D	2D	1D	2D
...	1	...	78	...	78	...
a	2	...	74	67	91	118
b	5	...	71	65	116	222
c	10	...	70	68	141	269
d	5	2	65	56	106	124
e	5	10	57	60	93	102
f	5[a]	...	60	48	97	189
g	20[b]	8	10	12	29	30
h	20[a]	8	12	8	36	31

[a] Radiative cooling model. One-dimensional velocities obtained using eq. (1) in the text.

[b] Adiabatic model with $\gamma = 1.01$. One-dimensional velocities obtained using eq. (2) in the text.

4.2. *Asymmetry Ratio*

We have explored the effects of different asymmetry ratios in the density of the RSG wind by running our standard model with ratios of equator to pole density of 2 (model a), 5 (model b), and 10 (model c). In each case the angle-integrated mass-loss rate was kept constant. Figure 3 shows the structure of the shell when the ring has reached a radius of R_{eq} for each of these runs. As one might expect, the aspect ratio of the shell increases with increasing asymmetry. This change in aspect ratio is primarily due to an increase in the expansion of the lobe, while the expansion rate at the equator remains similar for all three simulations.

The expansion velocities for these and some following simulations are given in Table 2, along with the expansion velocities predicted using one-dimensional models. Because of the inaccuracy of reading parameters off Figure 5 of Chevalier & Imamura (1983), we have used one-dimensional adiabatic simulations to obtain the one-dimensional velocities in Table 2. Based on previous testing (see § 4.1), we expect these values to be comparable to the velocities given by the self-similar solutions of Chevalier & Imamura (1983). The expansion velocities at the equator found in the two-dimensional simulations are within 10% of the values given by the one-dimensional models. In all cases the two-dimensional ring expansion velocity is smaller than in one dimension. This is readily explained by a small decrease in the interior pressure at the equator due to the directed flow driven by the interior pressure gradients. The lobe velocities, on the other hand, are all much greater than the results of the one-dimensional models, owing to the large ram-pressure contribution of the interior flow.

The ring expansion velocity does not change substantially between the models with different wind asymmetries. This is not unexpected, since the wind density on the equator differs by only 20% between our models. From the one-dimensional simulations this translates into only a 5% difference in expansion velocity for adiabatic winds. The largest density difference occurs along the pole, and hence the lobe expansion velocity is much higher in the large asymmetry models. This variation with asymmetry is enhanced by the added contribution of the ram pressure from the interior flow. While the one-dimensional

FIG. 3.—Adiabatic shell structure as a function of RSG wind asymmetry. The equator-to-pole density ratio in the three simulations is 2 (*left*), 5 (*middle*), and 10 (*right*) corresponding to models a, b, and c in Table 2. The simulations are shown at an age when the outer shock at the equator has reached a radius of 6.3×10^{17} cm, corresponding to times of 9.25×10^{10} s (*left*), 1.01×10^{11} s (*middle*), and 9.65×10^{10} s (*right*). Density contours are spaced at logarithmic intervals of 2.

models predict a difference of 50% in the expansion of the lobes between the low- and high-asymmetry models, the two-dimensional simulations show a difference of over 200%. By the time the equator-to-pole density ratio reaches 10, the interaction region resembles a jet outflow more than a spherical wind.

4.3. *Asymmetry Function*

Motivated in part by the large equatorial expansion velocities for the standard model compared with observations of the ring around SN 1987A, we have explored the effects of more severe asymmetry functions, $\dot{M}_r(\theta)$. In addition to the standard function given by equation (3), we have tried the asymmetry function used by Icke et al. (1992), but inverted to give a narrow peak in $\dot{M}(\theta)$ on the equator rather than a narrow trough along the pole. This function is

$$\dot{M}(\theta) = C\dot{M}_r\left[1 - A\,\frac{\exp(-2\beta\cos^2\theta) - 1}{\exp(-2\beta) - 1}\right], \qquad (4)$$

where β is a steepness parameter such that $\beta \approx 1$ gives a function similar to our standard function, while $\beta \gg 1$ gives a mass-loss function strongly peaked on the equator. The normalization constant C for the two runs described below is 1.84 for $\beta = 2$ (model d), and 2.80 for $\beta = 10$ (model e). Figure 4 graphs these functions to show the extreme behavior compared with the standard asymmetry function. For a given average mass-loss rate and pole-to-equator density ratio, a steeper mass-loss function (larger value of β) has a higher mass-loss rate on the equator and the pole and a lower mass-loss rate at midlatitudes (see Fig. 4).

The structure of wind bubbles created within winds following this asymmetry function is shown in Figure 5. The standard model is included for comparison, and each simulation is shown at an age when the forward shock at the equator has reached R_{eq}. The expansion velocities for the wind bubble at the equator and pole are given in Table 2. Because of the higher densities at both the pole and equator compared with the standard model, the expansion velocities are smaller and the wind bubble is more compact (Fig. 5*c*). This is accentuated by the two-dimensional hydrodynamics, which conspire to increase the expansion of the lobe in the standard model via internal ram pressure, but not in a wind bubble within a steep wind. For both the equatorial and the lobe expansion, the velocities found in the two-dimensional models are within 20% of the values obtained in the one-dimensional models. For steep mass-loss functions the interior flow is directed at the shell at midlatitudes, resulting in a stubby, flat-top wind bubble, but not affecting the ring or lobe expansion velocities. Note that for large values of β the high-density ring is much more compact than in the standard models. Aside from some gas being pulled upward by the interior flow, the height of the ring is even less than the radial width of the ring.

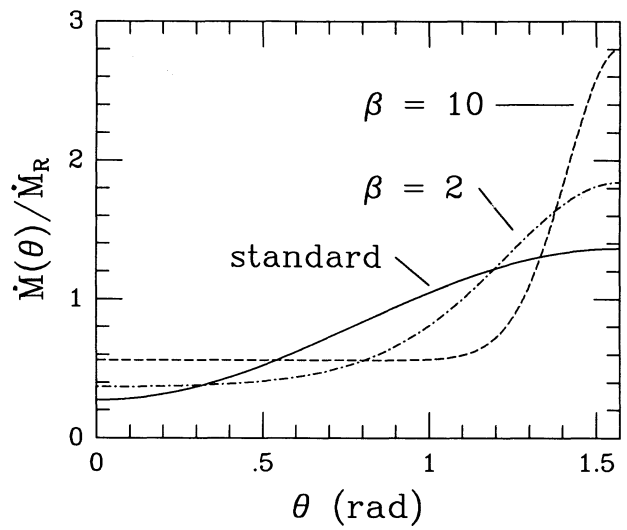

FIG. 4.—Angular variation of mass-loss rate in the RSG wind for the different asymmetry functions used in the text. In each case the equator-to-pole density ratio is 5. The solid line is the standard model function given by eq. (3) in the text. The other two lines are given by eq. (4) with the value of the steepness parameter as labeled.

4.4. *Radiative Cooling*

While we have so far limited our idealized numerical simulations to adiabatic winds, radiative cooling will be very important in the real problem of interacting winds. The effects of cooling have been discussed briefly by LM, who find that the forward shock along the pole is strongly radiative for the entire evolution of the shell, while the forward shock along the equator becomes adiabatic after approximately 1000 years owing to the low shock velocity. The inner shock is always adiabatic for the standard model because of the high shock velocity and low gas density. These results are based on much lower expansion velocities than we find in our simulations, so we will estimate the role of radiative cooling in our models.

Let us define a characteristic cooling time for the postshock gas,

$$t_{cool} \equiv \frac{kT}{n\Lambda}, \qquad (5)$$

where Λ is the cooling rate in ergs cm^3 s^{-1}, and t_{cool} is evaluated using conditions immediately behind the leading shock. We wish to compare this with the expansion time,

$$t_{exp} \equiv R/s, \qquad (6)$$

where R and s are the radius and expansion velocity of the shell, respectively. If we define $\xi \equiv t_{cool}/r_{exp}$, then for $\xi < 1$ the postshock gas cools before the shell can expand to lower densities where the cooling time is longer. Conversely, if $\xi > 1$ the shell expands to lower densities before the postshock gas can cool, increasing the cooling time, and resulting in an effectively adiabatic outer shock. In terms of wind parameters this parameter is

$$\xi = \frac{\pi\bar{m}kT_{sh}s_r v_r R}{\dot{M}_r\Lambda(T_{sh})}, \qquad (7)$$

where T_{sh} is the temperature immediately behind the outer shock. We can further define a critical radius R_c at which $\xi = 1$, such that for $R > R_c$ the outer shock is adiabatic ($\xi > 1$) and for $R < R_c$ the shock is strongly cooling ($\xi < 1$). If we evaluate this parameter for our standard model at both the pole and the equator, we find that $R_c \sim 3 \times 10^{21}$ cm at the equator (assuming $\Lambda \approx 10^{-20}$ ergs cm^3 s^{-1} for $s_1 \approx 60$ km s^{-1}; Shull & McKee 1979) and $R_c \sim 10^{18}$ cm at the pole (assuming $\Lambda \approx 2.5 \times 10^{-22}$ ergs cm^3 s^{-1} for $s_1 \approx 200$ km s^{-1}; Innes, Giddings, & Falle 1987). This implies that the outer shock at the ring is isothermal for all relevant times, while the rapidly expanding lobe is currently approaching the transition from isothermal to adiabatic. This result is due to the large

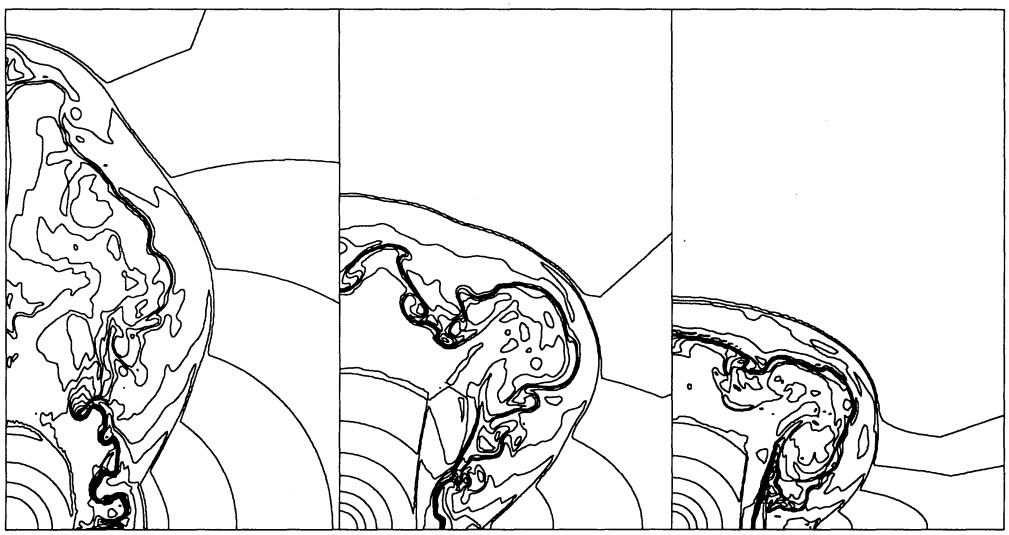

FIG. 5.—Adiabatic shell structure for RSG winds with different angular dependences of the wind mass-loss rate. The three simulations correspond to the three $\dot{M}(\theta)$ functions in Fig. 4: the left-hand image corresponds to the solid line in Fig. 4 (model b), the middle image to the dotted line (model d), and the right-hand image to the dashed line (model e). All three cases are shown at an age when the outer shock on the equator has reached 6.3×10^{17} cm, corresponding to $t = 1.01 \times 10^{11}$ s (*left*), $t = 1.36 \times 10^{11}$ s (*middle*), and $t = 9.87 \times 10^{10}$ s (*right*).

expansion velocity of the lobes found in the hydrodynamic simulations compared with the simple analytic models. At these high velocities the postshock gas is heated to over a million degrees, for which the cooling time is relatively long. At the equator the ring expansion velocities are sufficiently high that the postshock gas is at least partially ionized, resulting in very short cooling times.

The primary effect of cooling will be to collapse the already thin shell of shocked RSG wind into a very thin, dense shell. Because the gas motions within the shell are already very small in the adiabatic case, we do not expect much change in the structure of the interaction region other than a decrease in the width of this shell. The total column density in the shell should not change substantially, and the overall shape of the shell, which is determined by the hot shocked blue wind, should also remain similar. Dynamical instabilities of the nature discussed by Vishniac (1983) are likely to be important in the evolution of a cooled shell, and are expected to produce a very clumpy, nonuniform shell. While the analysis of Vishniac suggests that such a shell is marginally stable because there is no acceleration or deceleration, past experience with hydrodynamic simulations suggests that such dense, thin shells are always unstable (see, e.g., Stevens, Blondin, & Pollock 1992).

Unfortunately, we cannot adequately resolve the structure of such a thin shell with our numerical simulations. We have nonetheless run our standard model with a simple cooling function. Because of the lack of spatial resolution the shell does not reach the high densities and small dimensions expected with realistic cooling. The poorly resolved cooling region also removes energy from the hot shocked blue wind at the interface between the cooled RSG wind and the adiabatic BSG wind. The overall expansion of the shell may therefore be reduced due to the loss of thermal pressure from the interior. This simulation can, however, illustrate the role of increased dynamical instabilities and the similarity to the adiabatic simulations. We have used a grid of twice the resolution (400 × 400) to help reduce these errors. The energy loss is handled numerically by operator splitting the radiative cooling and the hydrodynamics, and the cooling is artificially reduced at the contact discontinuity separating the hot interior from the cold shell in order to reduce the errors associated with a poorly resolved cooling region (see Blondin, Fryxell, & Königl 1990 for details).

The exact cooling rates will be a complicated function of shock velocity and preshock ionization (e.g., Raymond 1979; Shull & McKee 1979) as well as the time history of the radiative shock (Innes et al. 1987). Furthermore, a normal interstellar cooling function with the cooling rate per unit volume increasing with n^2 will have an evolving cooling parameter, ξ, that may be very small at early times (leading to very large errors) even if it is near unity at late times. Rather than attempt to model the radiative cooling accurately when we know we cannot resolve the cooling region, we have employed a simple ad hoc cooling function that maintains a constant cooling parameter ξ throughout the expansion of the shell (i.e., $\Lambda \propto n^{-1/2}$). By setting the magnitude of such a cooling function in such a way that we are marginally resolving the cooling region, we can have the highest confidence in the accuracy of our simulations while approximating the evolution of a strongly cooling outer shock.

To test the numerical resolution of the radiatively cooling models, we ran a series of one-dimensional simulations with increasing values of the cooling function Λ (decreasing values of the cooling parameter ξ) on an expanding grid of 200 zones. The expansion velocity monotonically decreased with decreasing values of ξ and began to approach a constant expansion velocity of ~ 64 km s^{-1} at a cooling parameter of $\xi \sim 0.04$. This compares with a value of 65 km s^{-1} from equation (1). For smaller values of ξ the expansion velocity fluctuated around this value, with rather strong deviations occurring for very large cooling rates. Presumably these fluctuations in the velocity at very small values of ξ can be attributed to the poor resolution of the cooling region for such strong cooling. Based on these one-dimensional results, we believe that this ad hoc cooling function can accurately mimic strong cooling in the outer shock for values of ξ around 0.04 but not much less.

The structure of the standard model with radiative cooling (model f) included is shown in Figure 6, together with the adiabatic model at approximately the same physical size. The

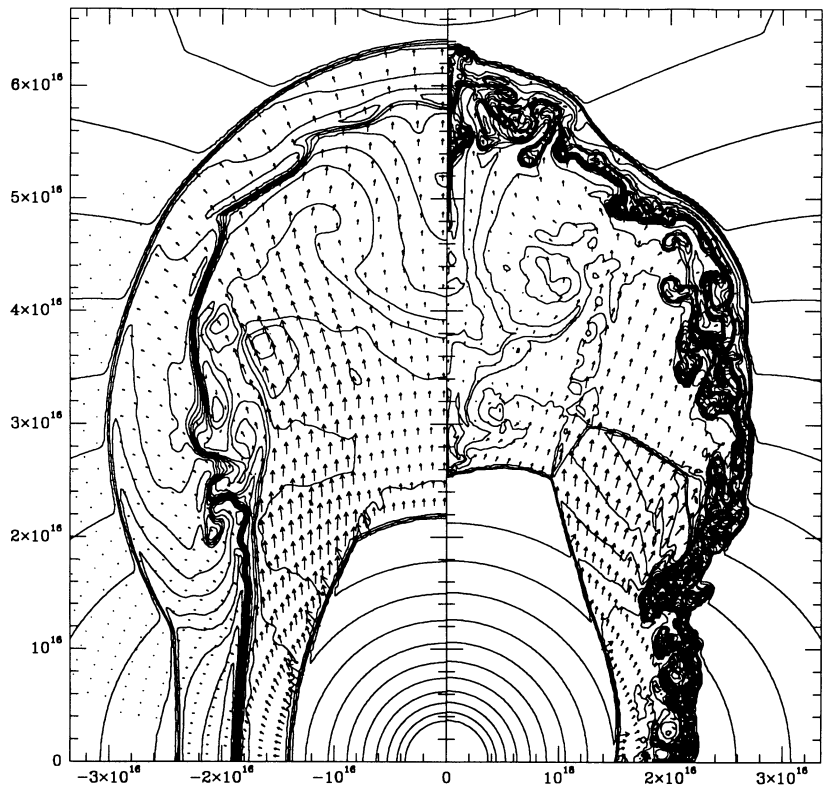

FIG. 6.—Shell structure for the standard model assuming adiabatic flow (*left*, model b) and strong radiative cooling (*right*, model f). The density contours are spaced in logarithmic intervals of $2^{1/2}$, and the velocity vectors are scaled the same in each plot.

expansion velocities at the equator are listed in Table 2. The expansion velocity is 20% less than the one dimensional estimate for the radiative run compared with only a 10% decrease between the one-dimensional and two-dimensional models. This low expansion velocity may be at least partially due to the loss of thermal energy from the shocked BSG wind in regions where the dense RSG wind is numerically diffusing into the hot interior of the shocked BSG wind. A similar phenomenon may occur in real wind bubbles through thermal conduction between the hot interior and the cool dense gas of the shell (see § 6).

The overall shape of the bubble is very similar in the adiabatic and cooling runs, including the asymmetry of the reverse wind shock. The primary difference is a very thin shell (which would be even thinner with higher numerical resolution) that appears to be dynamically unstable. As in the adiabatic simulations, the high pressure of the shocked BSG wind at the equator prevents the formation of any cusp as seen in the Kompaneets models.

5. A MODEL FOR THE SN 1987A RING

There is a striking difference between the observed expansion velocity for the ring, which is ~ 10.3 km s^{-1} (Crotts & Heathcote 1991), and the calculated equatorial velocity of the interaction region between the BSG/RSG winds in the previous section. Assuming adiabatic gas flow, we found that the latter velocity is $v_{eq} \sim 60$–70 km s^{-1}, regardless of the asymmetry function used and/or the ratio of equatorial to polar mass-loss rate during the RSG phase. Radiative cooling in the shocked RSG wind was not able to reduce the expansion velocity substantially. This result suggests that the standard model cannot explain the observed properties of the circumstellar shell around SN 1987A.

In order to derive a viable colliding winds model for the formation of the ring and lobes surrounding SN 1987A, let us use the results of the previous section along with the observational and theoretical constraints on the properties of the progenitor stellar winds. The results of the two-dimensional hydrodynamic models imply that the radial expansion of the ring is well modeled by one-dimensional hydrodynamics; nonradial motion contributes to a reduction of the ring velocity by no more than 10% for the parameters used in § 4. Moreover, given that the circumstellar shell has expanded by at least two orders of magnitude, we expect that the ring has reached a constant self-similar expansion velocity (cf. LM). This conclusion is borne out by the numerical simulations but is dependent on the assumption of constant wind velocities. We can therefore apply a one-dimensional analysis to find the expected velocity and Mach number of the ring expanding into the RSG wind and the postshock temperature and density. By fitting these properties to observations, we will find that rather extreme wind properties are required to make the colliding winds model workable.

5.1. *Observational Constraints on Wind Properties*

The BSG wind density is proportional to $\dot{M}_b/v_b$. An estimate of this ratio can be derived from the early radio emission from the supernova (Chevalier & Fransson 1987) using Chevalier's (1984) model for the evolution of the radio emission. In this model the radio emission is generated at the shock interface between the SN blast wave and the BSG wind where relativistic electrons are likely to be accelerated, producing syn-

chrotron emission. Shortly after the SN outburst the radio emission is absorbed by the unshocked BSG wind overlaying the SN blast wave. Eventually the SN will propagate out to a radius where the free-free optical depth of remaining BSG wind is less than unity and the radio emission will escape. The result is a turnover in the radio light curve at this epoch. The time between the explosion and the turnover provides a measure of the density in the wind. Unlike strong radio SNs such as SN 1979C and SN 1980K (cf. Weiler et al. 1986), the turnover for SN 1987A occurred only a few days after the SN explosion. Although the time of turnover is primarily set by wind density, the temperature of the wind is also important for this analysis. Lundqvist & Fransson (1991) calculated the temperature structure of the BSG wind around SN 1987A and found that $\dot{M}_b/v_b$ is $3 \times 10^{-6}\ M_\odot\ \mathrm{yr}^{-1}/550\ \mathrm{km\ s}^{-1}$.

The velocity of the BSG wind can be estimated based on comparisons with early-type stars similar to the progenitor of SN 1987A. Because the SN 1987A precursor was a B3 Ia star (Walborn et al. 1989), v_b cannot be very much lower than 550 km s^{-1} (Underhill & Doazan 1982). The lowest value possible is a velocity slightly larger than the escape velocity. For a 15 $M_\odot$ star with a photospheric radius of 3×10^{12} cm, roughly the values for the SN 1987A precursor (Woosley 1988), this means $v_b \approx 260$ km s^{-1}. For radiatively driven winds, however, a more realistic escape velocity is for a slightly larger radius than the photospheric (e.g., Mihalas 1978). We take 300 km s^{-1} as a lower limit to v_b. This limits $\dot{M}_b$ to $\approx 1.5 \times 10^{-6}\ M_\odot$ yr^{-1}. We point out that this value for $\dot{M}_b$ is valid only close to the SN. The early radio emission (Turtle et al. 1987) fell below detectability around day 30, corresponding to a radius of the blast wave of order 10^{16} cm (cf. Chevalier 1987). The ratio of $\dot{M}_b/v_b$ at larger radii, i.e., relevant to the colliding winds model, may be different from the value given by Lundqvist & Fransson (1991) if the mass loss of the BSG was not constant in time.

An estimate of $\dot{M}_b/v_b$ farther out in the BSG wind can be obtained if the currently observed radio emission (Staveley-Smith et al. 1992) is a result of the SN blast wave interacting with a density enhancement in the BSG wind (Chevalier 1992b). In this case the radius inferred from radio observations can be compared with the theoretical radius of the SN blast wave, $R_{\rm bw} \propto (\dot{M}_b/v_b)^{-0.13}$ (Chevalier 1987). This can only be considered a rough limit on $\dot{M}_b$ because of the weak dependence of $R_{\rm bw}$. For $\dot{M}_b = 6 \times 10^{-6}\ M_\odot\ \mathrm{yr}^{-1}$ and $v_b = 550$ km s^{-1}, Chevalier (1992b) finds that the radius of the SN blast wave was $R_{\rm bw} \sim 2.7 \times 10^{17}$ cm at the moment the observed radio structure had a radius of $(3\text{–}4) \times 10^{17}$ cm (i.e., in 1991 June and July). Given the dependence on $\dot{M}_b/v_v$, a value of $\dot{M}_b = 5 \times 10^{-7}\ M_\odot\ \mathrm{yr}^{-1}$ together with $v_b = 300$ km s^{-1} may actually correspond better to the extent of the observed radio structure. Although Chevalier attributed the cause of the radio emission to the interaction of the SN blast wave with the termination shock in the BSG wind, this estimate of $\dot{M}_b$ is also valid if the BSG wind is cooling. For v_b as low as 300 km s^{-1} this might actually be the case (see § 5.3).

For the RSG wind the upper limit to $\dot{M}_r/v_r$ is rather uncertain. In the spherically symmetric models of Lundqvist & Fransson (1991), the unshocked RSG wind emits late ($t > 400$ days) N v λ1240 roughly at the level that is now observed (G. Sonneborn 1992, private communication) if $\dot{M}_r/v_r$ is around, or slightly in excess of, $10^{-5}\ M_\odot\ \mathrm{yr}^{-1}/10$ km s^{-1}. However, as is demonstrated in § 6.1, only a rather modest mass loss is required to achieve an optically thick lobe. Since the fraction of gas ionized to N v or higher is relatively small, the N v λ1240 emission does not pose a serious constraint on M_r/v_r in our models.

A more direct estimate of $\dot{M}_r/v_r$ arises from the fact that the RSG wind is unlikely to contain more than $\sim 10\ M_\odot$ (e.g., Woosley 1988). With an outer limit of $\sim$4–5 pc (Chevalier & Emmering 1989) and a total wind mass of 10 $M_\odot$, this limit is $\dot{M}_r/v_r < 2.6 \times 10^{-5}\ M_\odot\ \mathrm{yr}^{-1}/10$ km s^{-1}. There is, however, the possibility that the RSG had a higher mass-loss rate the more it evolved, i.e., $\dot{M}_r$ is higher at radii corresponding to the observed ring than it is at larger radii. As a reasonable upper limit we choose $5 \times 10^{-5}\ M_\odot\ \mathrm{yr}^{-1}/10$ km s^{-1} for the late stages of the RSG evolution.

The expected value for v_r is $\sim$5–20 km s^{-1} (Zuckerman 1980). For the SN 1987A progenitor RSG wind, however, the wind velocity must be less than the observed ring expansion velocity of 10.3 km s^{-1}. If the wind was faster than the ring expansion, there would not be a shock expanding into the RSG wind and no shock compression to create the high densities of the observed ring.

5.2. *Implications of the Density and Velocity of the Ring*

The observed properties of the circumstellar shell around SN 1987A can be used to put stringent limits on the progenitor wind properties in the context of the colliding winds model. These properties include the expansion velocity of the ring, the density of the gas within the ring inferred from the UV and optical line emission, and the observed shell geometry, including the compactness of the ring and the ratio of the lobe radius to the ring radius (see § 6.1).

The density of the shocked RSG wind can be derived in terms of the wind parameters by assuming strictly radial flow. Dalgarno & McCray (1972) find that the interstellar cooling rate drops quickly below 200–500 K, depending on the relative fraction of free electrons in the gas. We assume that the unshocked RSG wind is a monatomic gas in thermal equilibrium at a temperature T_r in this range. Given the low wind velocity, the Mach number for the leading shock wave is therefore relatively low. We find $\mathcal{M}_1 \sim 3.4(T_r/200\ \mathrm{K})^{-1/2}(v_{\rm eq} - v_r)/5$ km s^{-1}, which limits v_r to be less than 8.8 km s^{-1} (8.0 km s^{-1}) for $T_r = 200$ K (500 K) in order for a shock to form. The postshock temperature is

$$T_2 \approx 7.4 \times 10^2 \left(1 - \frac{1}{5\mathcal{M}_1^2}\right)\left(1 + \frac{3}{\mathcal{M}_1^2}\right)\left(\frac{v_{\rm eq} - v_r}{5\ \mathrm{km\ s}^{-1}}\right)^2 \mathrm{K}\,. \quad (8)$$

Note that this temperature is not high enough for the postshock gas to be ionized. Between a few hundred and 1000 degrees the cooling rate is of the order of 10^{-26} ergs cm^3 s^{-1} (Dalgarno & McCray 1972). At a radius of 6.3×10^{17} cm, the cooling time scale for the shocked RSG wind, as defined in § 4.4, is

$$t_{\rm cool} \approx 5.4 \times 10^2 \left(\frac{v_{\rm eq} - v_r}{5\ \mathrm{km\ s}^{-1}}\right)^2 \left(\frac{v_r}{5\ \mathrm{km\ s}^{-1}}\right) \times \left(\frac{\dot{M}_r}{10^{-5}\ M_\odot\ \mathrm{yr}^{-1}}\right)^{-1} \mathrm{yr}\,. \quad (9)$$

The cooling time is thus less than the age, and radiative cooling is expected to be important for the postshock structure. The final postshock density is the result of both compression in the adiabatic shock and compression due to radiative cooling at roughly constant pressure behind the shock. The adiabatic compression ratio is given by $n_+/n_0 = 4/(1 + 3/\mathcal{M}^2)$, and the

additional compression due to cooling is $\sim T_2/200$ K. This combination gives a final postshock density at the radius of the observed ring of

$$n_{\rm post} \approx 147\left(\frac{\dot{M}_r}{10^{-5}\,M_\odot\ {\rm yr}^{-1}}\right)\left(\frac{v_r}{5\ {\rm km\ s}^{-1}}\right)^{-1}\left(\mathcal{M}^2-\frac{1}{5}\right){\rm cm}^{-3}\,. \quad (10)$$

With the upper limit for $\dot{M}_r/v_r$ given in § 5.1 and $v_r = 5$ km s^{-1}, we get a rough upper limit to the present value of $n_{\rm post} \approx 3.8 \times 10^3$ cm^{-3} (1.5×10^3 cm^{-3}) for $T_r = 200$ K (500 K). This value can be increased by assuming a strong asymmetry in the wind, such that the mass-loss rate along the equator is substantially higher than the average wind density that is restricted by the limits given in § 5.1. On the other hand, we do not expect $n_{\rm post}$ to be higher than the density inferred from the presently observed optical line emission, $n \sim 7 \times 10^3$ cm^{-3} (Wang 1991), or at least the density of the gas emitting the UV lines, $n \sim 2 \times 10^4$ cm^{-3} (Lundqvist & Fransson 1991).

We note that LM do not require a large $\dot{M}_r(\pi/2)$ by having the ring decelerating with time, so that at earlier times the velocity was sufficiently large, and the postshock temperature sufficiently high, that radiative cooling produced much more compression. This deceleration of the ring appears to be an artifact of the formation of a cusp, and since we do not expect a cusp to form when the full hydrodynamical equations are considered, we do not consider this possibility further.

In order to obtain a low equatorial expansion velocity comparable to the expansion rate of the observed ring, we note that the lowest shell expansion rate is found for the case of strong cooling in both winds. If we take this as a limiting case and use the BSG wind parameters with the minimum momentum ($\dot{M}_b = 1.5 \times 10^{-6}\ M_\odot$ yr^{-1}, $v_b = 300$ km s^{-1}) and a RSG wind velocity of 5 km s^{-1}, we get a lower limit on the RSG wind mass-loss rate of $\dot{M}_r \sim 8 \times 10^{-5}\ M_\odot$ yr^{-1}. For the standard BSG wind parameters this is increased to $\dot{M}_r \sim 2.9 \times 10^{-4}\ M_\odot$ yr^{-1}. The low expansion rate of the ring, and the high densities in the ring, force us to the same conclusion: the RSG wind mass loss rate was extremely high.

5.3. *A Viable Colliding Winds Model*

To arrive at a working colliding winds model for the formation of the circumstellar shell surrounding SN 1987A, we are apparently forced to assume relatively extreme values for the progenitor wind parameters. The low expansion velocity of the ring requires a low momentum flux in the BSG wind and a very massive, slow RSG wind. A second constraint is implied by the low expansion velocity coupled with the observed high gas density in the ring; the RSG wind must be very dense along the equator. In order to satisy these requirements and at the same time avoid the strong theoretical limits on the average mass-loss rate of the RSG wind, we are forced to propose a very large asymmetry in the RSG wind. A very asymmetric RSG wind is nonetheless consistent with the size of the bipolar lobes seen in the NTT images. Following these arguments, let us "construct" a colliding winds model that could match the observations. As a guide through this discussion we make use of Table 3, where we have calculated various parameters with equations (1), (2), and (10) for $v_r = 3$, 5, and 7 km s^{-1} and $v_b = 300$ km s^{-1}. While these equations assume one-dimensional flow, we know from Table 2 that these estimates should prove sufficient to construct a full two-dimensional model.

To begin with, let us assume that the BSG wind has the lowest velocity that our previous estimates allow, $v_b = 300$ km s^{-1}. For such a slow wind this raises the possibility that the shocked BSG wind is able to cool radiatively, a situation that was not considered for the fast BSG wind ($v_b = 550$ km s^{-1}). The cooling parameter for the shocked BSG wind is $\xi_b \approx (\dot{M}_b/10^{-6}\ M_\odot\ {\rm yr}^{-1})^{-1}(R_{\rm in}/2.9 \times 10^{17}$ cm), where $R_{\rm in}$ is the radius of the inner shock and we have used a cooling rate of $\Lambda = 10^{-22}$ ergs cm^3 s^{-1} appropriate for a shock velocity of ~ 300 km s^{-1} (Gaetz & Salpeter 1983). The shocked BSG wind is able to cool on a short time scale early in the evolution of the circumstellar shell. At the present epoch ($R_{\rm in} = 6.3 \times 10^{17}$ cm) the BSG wind may be going through a transition from radiatively cooling to adiabatic flow for the values of $\dot{M}_b$ quoted in § 5.1. The transition from rapidly cooling to adiabatic flow is not expected to occur rapidly, for at least two reasons. First, the cooling parameter is only linear in radius and the shell must expand more than an order of magnitude to go from very strong cooling to almost adiabatic flow. Second, as the BSG wind becomes adiabatic, the reverse shock will push inward to regions of higher density and hence increased cooling, slowing the changeover to adiabatic flow even more.

From the above expression for the cooling parameter we find that for $v_b = 300$ km s^{-1} it is required that $\dot{M}_b \gtrsim 2 \times 10^{-6}\ M_\odot$ yr^{-1} for the shocked BSG wind to be radiatively cooling at present. In this case we can use the ram-pressure equation to derive the mass-loss rate from the RSG required to produce the observed equatorial expansion. Solving equation (2) with $\dot{M}_b = 1.5 \times 10^{-6}\ M_\odot$ yr^{-1} and a RSG wind velocity of 5 km s^{-1}, we get an equatorial mass-loss rate of $\dot{M}_r(\pi/2) = 7.5 \times 10^{-5}\ M_\odot$ yr^{-1} (see Table 3 for dependence on v_r). From Table 3 we see that this value is consistent with the requirement that the postshock density be $\sim 7 \times 10^3$ cm^{-3} if $T_r \sim 500$

TABLE 3

PARAMETERS FOR COLLIDING WINDS MODEL

v_r (km s^{-1})	$f_{\rm adia}$	$f_{\rm cool}$	$\mathcal{M}_1$	n_+/n_0	$n_{\rm post}/n_0$	$\dot{M}_r(\pi/2)$ ($M_\odot$ yr^{-1})
3.....	6.1×10^{-3}	6.4×10^{-2}	5.0 (3.2)	3.6 (3.1)	31 (12)	1.1×10^{-5} (2.9×10^{-5})
5.....	1.9×10^{-3}	2.0×10^{-2}	3.6 (2.3)	3.3 (2.6)	16 (6.4)	3.6×10^{-5} (7.5×10^{-5})
7.....	5.3×10^{-4}	5.6×10^{-3}	2.3 (1.4)	2.5 (1.6)	6.2 (2.3)	1.4×10^{-4} (3.6×10^{-4})

NOTE.—Parameters describing a colliding winds model as a function of RSG wind velocity, v_r, for an equatorial expansion velocity of 10.3 km s^{-1}. The BSG wind velocity is $v_b = 300$ km s^{-1}, and the RSG wind temperature is 200 K (500 K for values in parentheses). The parameters $f_{\rm adia}$, $f_{\rm cool}$ are the ratios of $\dot{M}_b/\dot{M}_r(\pi/2)$ required to produce the observed equatorial expansion velocity for models in which the shocked BSG wind is adiabatic and radiatively cooling, respectively. The mass-loss rate in the equatorial plane, $\dot{M}_r(\pi/2)$, is calculated assuming a postshock density of $n_{\rm post} = 7 \times 10^3$ cm^{-3}.

K. A lower T_r would result in a higher density in the ring. To achieve a lobe expansion roughly 3 times faster than the equatorial expansion would require a polar mass-loss rate of $\dot{M}_r(0) \approx 4 \times 10^{-6}\ M_\odot\ \mathrm{yr}^{-1}$, translating into an equator-to-pole density ratio of ~ 20.

If the RSG wind is held at a constant temperature during its expansion, a very high equator-to-pole density ratio would result in an overpressure along the equator compared to the poles. This overpressure will expand the high-density equatorial region at approximately the Mach angle as the wind expands into the surrounding medium. If all the extra mass loss were concentrated in the equatorial plane near the source of the wind, the high-density region would fill a cone of width $\sim 1/\mathcal{M}_r$ at large radii. Assuming a wind temperature of 200 K, the Mach number of the wind is $\mathcal{M}_r \approx 3.6$ for 5 km s^{-1} (see Table 3), corresponding to an opening half-angle of $\sim 16°$. A steepness parameter of ~ 10 in equation (4) will give a mass concentration within this half-angle. Using $\beta = 8$ and the above mass-loss rates, the average mass-loss rate is $\langle \dot{M}_r \rangle = 2 \times 10^{-5}\ M_\odot\ \mathrm{yr}^{-1}$, close to the limits found in § 5.1.

To check the validity of such an extreme model in terms of the morphology of the circumstellar ring and lobes, we have used our two-dimensional hydrodynamics code to evolve a wind bubble into a RSG wind with the parameters given above. Since both winds are strongly cooling in this model, we have opted to use an adiabatic exponent γ close to unity rather than attempt to model the radiative cooling directly. This is only an approximation, as a radiatively cooling gas with a cutoff in the cooling rate at some floor temperature does not behave the same as an ideal gas with $\gamma = 1$. In particular, when the gas flow diverges the pressure remains constant in the $\gamma = 1$ case, but in the cooling case the temperature may drop below the floor value and the pressure will drop, providing a resistance to the divergent flow. Nonetheless, we expect the qualitative conclusion of this model to hold for the corresponding case of a radiatively cooling gas: dynamical instabilities severely deform the circumstellar shell. Figure 7 shows the structure of the resulting wind bubble for $\gamma = 1.01$ (model g) when the equatorial ring is at a radius of 6.3×10^{17} cm. In contrast to all the previous models, the outer surface of the stellar wind bubble is not round. The expansion velocities for this model are given in Table 2, and are relatively close to the values predicted by the one-dimensional models.

While this model produces the correct expansion velocity and ring density, we find it unsatisfactory for two reasons: the unstable nature of the circumstellar shell and the lack of a reverse shock at small radii. When both stellar winds cool rapidly behind the wind shocks, the thin, dense circumstellar shell appears to be dynamically unstable. This instability has not been investigated in detail, but has been seen in other numerical simulations (Stevens et al. 1992). In essence, the strong radiative cooling removes the isotropic thermal pressure that would otherwise smooth out any perturbations growing in the region between the two shocks. The consequence of this instability is a very nonuniform shell with very extended protrusions, particularly around a polar angle of 50°–60° (see Fig. 7). This picture is inconsistent with the smooth structure observed by the NTT, implying that the BSG wind is, at least at present, partially adiabatic.

The second complication is the lack of a reverse wind shock. As seen in Figure 7, the radiative energy losses of the BSG wind collapse the reverse wind shock onto the contact discontinuity. This means that there is no wind shock at small radii to explain the turn-on of the radio emission around day 1300 as in the model proposed by Chevalier (1992b). If the shocked BSG wind is radiative, the late radio emission must be caused by the interaction of the blast wave with a density enhancement in the unshocked BSG wind created in some other way than by the termination shock (see § 6.2).

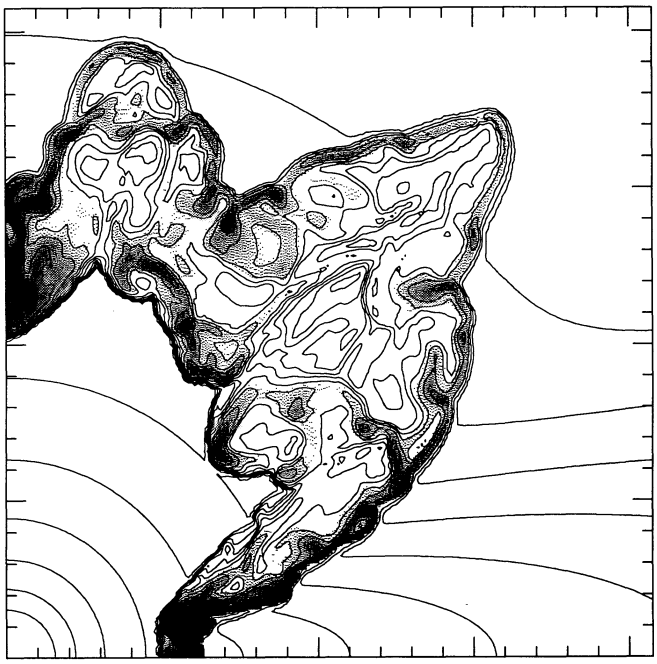

FIG. 7.—Shell structure for the nonstandard model using $\gamma = 1.01$ and a RSG wind with equator-to-pole density ratio of 20 and a steepness parameter of $\beta = 8$ (model g). The density contours are spaced in logarithmic intervals of 2. The highest density shocked gas is shaded in black to highlight the dense shells formed behind the forward and reverse wind shocks.

Both of these "reservations" are avoided if the BSG wind is adiabatic. However, in order to have an adiabatic BSG wind and a slow ring expansion, we must postulate a very low $\dot{M}_b$. This is required both to minimize the momentum in the BSG wind and to ensure a low enough density that the BSG wind is adiabatic. As mentioned in § 5.1, a value as low as a few times $10^{-7}\ M_\odot\ \mathrm{yr}^{-1}$ may be reasonable if the BSG mass loss was much lower at earlier times.

To construct an adiabatic BSG wind model, let us begin with the same RSG wind parameters as in the last model. Assuming a minimum BSG wind velocity of $v_b = 300$ km s^{-1}, we can use equation (1) (or Table 3) to find the BSG mass-loss rate needed to produce an equatorial expansion velocity of 10.3 km s^{-1}: $\dot{M}_b \approx 1.5 \times 10^{-7}\ M_\odot\ \mathrm{yr}^{-1}$. Because we are beginning to approach the limit of an isobaric interior, the pressure behind the equatorial ring is expected to be slightly lower than implied by this one-dimensional estimate, and we can use a slightly larger value of $\dot{M}_b$ to get the desired expansion velocity. For the model shown in Figure 8 (model h) we used $\dot{M}_b = 3 \times 10^{-7}\ M_\odot\ \mathrm{yr}^{-1}$. The strong cooling in the outer shock was modeled numerically as described in § 4.3. We ran this simulation only until the expansion velocities settled into their steady state values. We have found that the radiative cooling runs tend to collect cold gas on the symmetry axis at late times, which may influence the expansion velocities. Given the self-similar nature of the flow, we expect the circumstellar shell to remain qualitatively the same past the time shown in Figure 8.

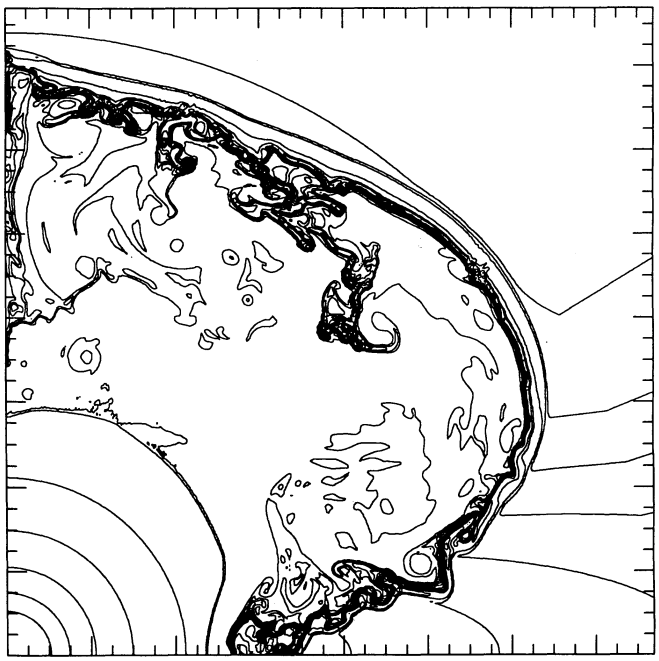

FIG. 8.—Shell structure for the nonstandard adiabatic BSG wind model with a radiatively cooling RSG wind with equator-to-pole density ratio of 20 and a steepness parameter of $\beta = 8$ (model h). The density contours are spaced in logarithmic intervals of 2.

The expansion velocity along the equator in model h is much less than the one-dimensional estimate given by equation (1) (see Table 2). While this may be due in part to the loss of thermal energy from the interior due to numerical error (see § 4.4), we believe it primarily is due to the effects of an isobaric interior. The pressure variations within the shocked interior are less than a factor of 3. This is a direct result of the low expansion velocity compared with the canonical model of LM; the ratio of interior sound speed to expansion velocity is greater than 20 in model h, compared with a factor of 4 for the canonical wind parameters. The rapid sound speed allows the shocked gas along the equator to relax into the bubble interior, reducing the overpressure along the axis. The pressure driving the shell at the equator is thus less than implied by the one-dimensional estimate, resulting in a slower expansion velocity. In effect, the Kompaneets approximation is not bad for these wind parameters.

Figure 8 illustrates the dynamical instability of the thin shell of cooled RSG wind. Near the equator, where our ad hoc cooling function produces the smallest cooling length, the shell as a whole is unstable. Near the top of the lobe, where the cooling length is a few times larger, the dominant instability is a shearing of the inner surface of the shell. Both of these instabilities, although the later more so, will tear off blobs of the dense shell gas and mix them into the interior. In the presence of thermal conduction we expect these blobs to evaporate relatively quickly (see § 6). This model is still dynamically young with respect to these instabilities, and we would expect an older shell to show more drastic signs of instability. We also expect the shell instability that is responsible for the kinks in the shell near the equator to operate over the entire shell. Our model produces an artificially large cooling length for the forward shock away from the equator, and this tends to suppress the shell instability. Realistically, the cooling length will be very small over the entire surface of the circumstellar shell.

The circumstellar shell in Figure 8 provides a reasonably good fit to the observed shell around SN 1987A. There is a high-density, compact ring at the equator, and a thin, clumpy shell that extends out to 2–3 times the radius of the ring. Note that the accumulation of dense gas on the symmetry axis is an artifact of the imposed symmetry (see § 4.1). A detailed comparison of this and other models with the observations of SN 1987A, including the effects of time- and density-dependent degree of ionization, light travel time, and optical depth, will be presented in Lundqvist, Fransson, & Blondin (1993).

6. DISCUSSION

The working model described in § 5 is simply that—a model of the hydrodynamic interaction between a BSG wind and an asymmetric RSG wind that produces many of the observed characteristics of the circumstellar shell surrounding SN 1987A. Within this idealized model, the parameters of model h are only representative of the possible parameters for the progenitor of SN 1987A. In particular, the form of the asymmetry in the RSG wind and the magnitude of the density ratio used in this model were found to produce a circumstellar shell in reasonably good agreement with observations. There are undoubtedly other forms for $\dot{M}_r(\theta)$ that produce similar results, although we expect that a density ratio of at least 10 is required. Similarly, the temperature, velocity, and mass-loss rate of the RSG wind can all be varied to some degree and still produce a circumstellar shell in accord with observations. Our primary result is that a very large $\dot{M}_r$ strongly concentrated to the equator and a relatively small $\dot{M}_b$ are required to explain the observations.

This idealized model does not address several effects that may be relevant to the formation of the circumstellar shell of SN 1987A, including thermal conduction, time variation of the progenitor winds, and lack of axisymmetry. Thermal conduction can be expected to transport heat from the hot, adiabatic interior into the cold, dense shell of shocked RSG wind, where it is efficiently radiated away. This physical process has the same effect as the numerical error generated by the radiative cooling term in the vicinity of the contact discontinuity (§ 4.4): the removal of thermal energy from the hot interior, thereby decreasing the pressure driving the expansion of the circumstellar shell. Given the uncertainty in estimating the conductive heat flux (e.g., surface area, thermal gradients, magnetic suppression, etc.), we can only say that thermal conduction may in fact be important in the dynamics of the colliding winds model. In the limit that thermal conduction is fast enough to remove all of the thermal energy of the shocked BSG wind, we have the same situation as in the isothermal BSG wind model. In this sense, we can regard our isothermal model (model g) as a limiting case.

All of our simulations have assumed constant progenitor wind parameters, more from lack of information than from any theoretical prejudice. In fact, our working model with $\dot{M}_b = 3 \times 10^{-7}\ M_\odot\ \mathrm{yr}^{-1}$ and $v_b = 300\ \mathrm{km\ s}^{-1}$, together with the estimates of $\dot{M}_b/v_b$ by Lundqvist & Fransson (1991), imply that the mass-loss rate of the BSG wind increased more than an order of magnitude just prior to the SN explosion (on a time scale of less than 500 yr). In our models we have assumed that the transition from a RSG to the final BSG stage was relatively quick, so that the expanding shell has long since traversed the stellar wind generated during this transition. If, on the other

hand, the change in the mass-loss rate associated with this stellar transition lasted for more than $\sim 10^4$ yr, the temporal behavior of the wind may have affected the dynamics of the circumstellar shell.

Observations of the circumstellar shell of SN 1987A appear axisymmetric, and, indeed, we expect the stellar winds that formed the shell to be axisymmetric. However, the formation process might break this axisymmetry on both small and large scales. All of our two-dimensional hydrodynamic simulations have shown evidence for dynamical instabilities of some nature. This is particularly true for the radiative cooling models applicable to SN 1987A, where dynamical instabilities in the thin shell produced a very clumpy shell and several blobs of cool gas floating within the hot interior gas. Realistically, these instabilities will also operate in the third dimension, producing distinct blobs rather than the thin rings implied by our axisymmetric models. On a global scale, the presence of a large vortex in our two-dimensional models suggests that three-dimensional simulations may not retain the axisymmetry imposed in our simulations (see § 4.1).

Finally, let us discuss some observed features of the circumstellar shell that impact the viability of our model: specifically, the size of the lobes with respect to the light-echo paraboloid, the source of the late-time radio emission, the detection of Hα blobs coincident with the lobes, and possible sources of asymmetry in the RSG wind.

6.1. *The Lobes*

The loops around the supernova observed with the NTT on day 1036 (Wampler et al. 1990) had maximum extensions of roughly 2".5 away from the supernova to the north and slightly less to the south. The maximum extensions of the loops are thus roughly a factor of 3 larger than the radius of the ring observed with *HST*. The observed structure of the outer lobes does not appear to change appreciably with time. (E. J. Wampler & L. Wang 1992, private communication). This means that if the loops are interpreted as limb-brightened parts of a circumstellar shell such as is seen in our simulations, and if the ultimate energy source for this emission is the SN light, then the limbs must lie within the light-echo paraboloid on day 1036. In particular, this is the case for the continuum emission, which is mere dust reflection of SN light. For the line emission the recombination time to the observed ionization stages must also be taken into account. If this recombination time is not negligible compared with the epoch of the observations, the light-echo paraboloid must have swept by the limb earlier than day 1036, with the time difference being roughly equal to the recombination time.

To see what constraints this puts on our models, we assume a plane, A, cut through the observed ring which has its normal directed toward us. With a distance of 50 kpc to the SN, the 1036 day light-echo paraboloid encloses gas extending out to a projected radius of 2".5, i.e., the observed maximum lobe radius, only if the gas does not lie farther behind A than $\sim 6.9 \times 10^{17}$ cm. The lobes are thus only marginally enclosed by the light-echo paraboloid, and if we include the fact that the structure is tilted by 43°, it will be hard to account for significant recombination times if the rear lobe should be possible to observe.

There are two ways of explaining why the rear lobe may be seen in line emission on day 1036. Either recombination is very fast, or the gas is optically thick to the ionizing photons from the SN during its outburst, so that there are O III and N II zones emitting the observed lines without relying on recombination. In the latter case the density could be low ($< 10^3$ cm^{-3}). With a lobe radius of $\sim 2 \times 10^{18}$ cm, assuming pure radial compression of the RSG wind and using the results of Luo (1991) and Lundqvist et al. (1993) for the ionization structure, we find that $\dot{M}_r > 10^{-5}\ M_\odot\ \mathrm{yr}^{-1}$ to produce O III and N II zones.

One problem with the fast recombination case is that the UV line light curves dropped dramatically after 400 days, implying that gas outside the 400 day light-echo paraboloid does not contribute to the total UV line emission for these lines (Lundqvist & Fransson 1991). Such a contribution would be expected in the case of high-density gas in the lobes. If the lobe density is low, we find from the models of Lundqvist & Fransson (1991) that the only UV line contributing to the total emission should be N v λ1240. Indeed, N v λ1240 was still emitting roughly 10% of its peak value around day 1700 (G. Sonneborn 1992, private communication). We therefore find that a low-density, optically thick lobe component could more likely explain the observed structure in the forbidden lines, as well as account for part of the late N v λ1240 emission, than a model relying on fast recombination. This is consistent with our working model, for which the preshock RSG wind density is much lower off the equator than it is along the equator.

Two obvious ways of testing this would be to observe the time variation of the optical lobe emission and to image the N v λ1240 emission. In the low-density case, the forbidden line emission should decline much slower than the continuum emission, which is merely a dust reflection of the SN light. Also in the low-density case, the N v λ1240 emission should still be emitted by the lobes at the present epoch. A more detailed analysis of emission-line fluxes from the ring and lobes will be included in a future paper (Lundqvist et al. 1993).

6.2. *The Late Radio Emission*

As was pointed out in § 5.1, the late radio emission observed by Staveley-Smith et al. (1992) is most naturally explained by interaction between the SN blast wave and a density enhancement in the BSG wind. Chevalier (1992b) provides an attractive explanation of this emission in terms of the termination shock in the BSG wind. However, Chevalier made the simplified assumption of the shock being spherical. From our calculations we find that the termination shock is significantly elongated in the polar direction. We may estimate how this change of geometry affects Chevalier's results. In the case of a spherical shock, light-echo effects spread the observed sweeping up of the termination shock by the blast wave over roughly 200 days for parameters and expressions used in Chevalier (1992b). During this period (between day 1300 and day 1500) the sweeping-up rate is constant.

For our analysis we assume a cylindrically shaped termination shock with the ratio of radius to height of 1:4. We have weighted the swept-up structure by R^{-4} to account for the decrease in density with radius. Furthermore, the cylinder is tilted by 43° to the line of sight. With these assumptions, the sweeping-up rate peaks rather sharply around day 1450, and decreases to 25% of its maximum value in ~200 days and to 10% in ~500 days. Based on geometry alone, we therefore expect a somewhat longer period of radio emission than in the case of a spherical termination shock. In particular, this is expected if the generation of turbulence becomes more efficient when the blast wave and the plane of density enhancement become increasingly nonparallel with time, as in the cylindrical case. It is interesting to note that the radio observations show

an almost linear increase from day 1300 up to day 1900, which is a longer rise time than predicted in Chevalier's model (R. Chevalier 1992, private communication). This may point to a geometrical effect like the one just described. Mixed into the interpretation of a prolonged rise time may also be effects of the poorly known generation of synchrotron emission.

In the models with a radiatively cooling BSG wind the termination shock of the BSG wind lies on the inside surface of the outer lobes. In this case one must postulate some other source for the generation of the radio emission, such as a density enhancement created by a sudden change in the mass-loss rate of the presupernova star during its BSG stage; we see no evidence for density enhancements lagging the shell in our models. We cannot, however, rule out the possibility that three-dimensional modeling may reveal such features. White, Argue, & Van Leeuwen (1992) find that the weak spokelike structure in the *HST* picture (Jakobsen et al. 1991) coincides with the center of the radio emission. Apart from this, there are no signatures of density enhancements in the BSG wind in either UV line light curves, X-ray data (Serlemitsos et al. 1992), or other observations. As in the termination shock model, this may not be a problem (Chevalier 1992b) if the density contrast between the ejecta and the gas it strikes is not large. Otherwise, the shock velocity traversing the density enhancement would be much lower than the velocity of the ejecta, and the situation would resemble the model of Luo & McCray (1991) for the interaction between the ring and the ejecta. In this case we would expect detectable UV line emission from the interaction.

6.3. Hα *Blobs*

The *HST* picture (Jakobsen et al. 1991) shows that the ring is patchy, indicating that the ring is made of several blobs. Blobs have also been reported using ground-based telescopes. Crotts, Kunkel, & McCarthy (1989) observed two Hα spots, 2".0 and 2".3, north and south of the SN, respectively, around day 750 (see also Crotts & Heathcote 1991). No similar features were seen in [O III]. Hanuschik (1991) found an Hα spot 2".1 northwest of the SN around day 950. A similar feature was reported by Cumming & Meikle (1992) only 0".3 from the SN on days 1254 and 1344. This blob's Hα emission had a very narrow width, indicating a temperature of less than 10^3 K. The blob was seen also in Hβ. In addition to the hydrogen blobs, a blob displaced by 0".8 from the SN was observed in He I λ10830 by Allen, Meikle, & Spyromilio (1989) from day 570 until at least day 735. Crotts et al. (1989) did not find enhanced Hα emission at the position of the helium blob.

The blobs all seem to be rather transient features, with typical declining time scales shorter than for the ring. For example, the flux from the blob observed by Cumming & Meikle declined on a time scale of roughly 1 month. The general absence of [O III] spots probably indicates that the blobs at the moment of observations already had cooled to less than $\sim 10^4$ K. The fast cooling is likely to be a result of high densities, of order 10^4–10^5 cm^{-3}. However, not even for these densities is it possible to cool the gas to less than 10^3 K before the gas runs out of free electrons. We have used the time-dependent photoionization code in Lundqvist & Fransson (1991) to investigate this, using evolutions for the outburst spectrum described in Lundqvist (1992). We find that it is hard to cool the gas to less than 3×10^3 K with a pure atomic gas. It is therefore likely that dust cooling plays an important role in cooling the blobs (see also Cumming & Meikle 1992).

Most of the UV lines show very little emission after ~ 500 days. There are, however, indications of transient humps in the light curves from day 800 and onward (G. Sonneborn 1992, private communication). Although the fluxes are only slightly above noise level, it is interesting to note that such humps are expected for rapidly recombining, isolated blobs. The observed coincidence of all the blobs, except the 10^3 K one, with the NTT lobe makes it intriguing to suggest that the blobs are density enhancements in the circumstellar shell. This was also noted by Crotts & Heathcote (1991). Our conclusion is therefore that although the lobes generally consist of low-density gas (cf. § 6.1), there are also high-density blobs and dust mixed into this structure.

From our hydrodynamic simulations we find that such a structure is a natural consequence of the interacting winds model. When the outer shock is radiatively cooling, dynamical instabilities create a very clumpy shell, as seen in Figures 6 and 8.

6.4. *Cause of Asymmetry*

To arrive at models with equatorial expansion velocities close to the observed ring velocity, and at the same time avoid using extreme values for the average mass-loss rate $\dot{M}_r$, we found in § 5 that we are forced to postulate a rather extreme asymmetry in the RSG mass loss. This is in sharp contrast to the contention of WM that only a very small density contrast in the RSG wind is required to reproduce the observations.

As was noted by LM, it is unlikely that the wind asymmetry is in any way the result of a protostellar disk, since such a disk would have been evaporated by the BSG wind during the star's main-sequence evolution. Another argument against a protostellar disk is the high overabundance of nitrogen in the ring (Fransson et al. 1989), which clearly indicates that the gas is of stellar origin rather than interstellar. It is also unlikely that the asymmetry was caused by rapid rotation of an isolated star (e.g., Chevalier & Soker 1989). Conservation of angular momentum implies that a rapidly rotating main-sequence star will slow considerably during the expansion to the RSG stage, resulting in a very slowly rotating RSG and hence a spherical RSG wind.

The best candidate for producing a very asymmetric wind in the RSG stage is the influence of a binary companion. A close binary companion could affect the RSG wind during a phase of common envelope evolution (e.g., Livio & Soker 1988). The common envelope phase could either transfer the orbital angular momentum needed to spin up the RSG envelope so that stellar rotation might produce the asymmetric wind, or it could produce a short burst of rapid mass loss in the equatorial plane as the companion spirals into the core of the RSG. Another possibility is that a companion star in a relatively wide orbit could gravitationally focus the RSG wind into the orbital plane. A 1 $M_\odot$ companion at an orbital radius of 10^{15} cm, corresponding to an orbital period of hundreds of years, can influence a large fraction of a supergiant wind expanding at only 5 km s^{-1}. At present, however, there are no direct signs of a binary companion. In an evaluation of different ways to create the ringlike structure around SN 1987A and at the same time explain the spectroscopic features of the supernova's spectrum as well as its blue nature, Podsiadlowski (1992) argues for an accreting and/or a merging scenario. His arguments follow along the lines of likely explanations to the bipolar structure seen for some planetary nebulae (Morris 1981).

7. SUMMARY

We have modeled the nebulosity around SN 1987A in the context of the presupernova's BSG wind interacting with an asymmetric RSG wind. The strategy of calculation has been to employ a two-dimensional time-dependent hydrodynamics code based on the piecewise parabolic method. To explain the overall shape of the nebula, as well as the expansion velocity of the observed ring, we are forced to abandon parameters used in previous, simplified models (LM; WM). We find that a model with an average $\dot{M}_r \sim 2 \times 10^{-5}\ M_\odot\ \mathrm{yr}^{-1}$ and an equator-to-pole density ratio in the RSG wind of ~ 20 can adequately explain the observations. In this model the shocked RSG wind is radiatively cooling throughout the evolution, whereas the BSG wind has recently passed through a transition from radiatively cooling behind the termination shock to adiabatic throughout the flow. This model produces a lobe structure in qualitative agreement with the NTT images, and can explain the late radio emission, the average densities in the ring, and the slow expansion of the ring, as well as provide a qualitative explanation of the observed blobs coinciding with the lobes. The large asymmetry required in the RSG wind appears to suggest the presence of a binary companion at least during the RSG stage.

We thank Roger Chevalier, Ding Luo, and Lifan Wang for many fruitful discussions. The numerical simulations described in this paper were run on the Cray Y-MP/464 at the North Carolina Supercomputing Center. P. L. acknowledges a *Hubble Space Telescope* Fellowship under contract HF-1015.01-90A. J. M. B. acknowledges support by NSF grants PHY90-57865 and PHY90-01645.

REFERENCES

Allen, D. A., Meikle, W. P. S., & Spyromilio, J. 1989, 342, 403
Arnett, W. D. 1988, in Proc. of the Fourth George Mason Workshop, Supernova 1987A in the Large Magellanic Cloud, ed. M. Kafatos & A. G. Michalitsianos (Cambridge: Cambridge Univ. Press), 301
Blondin, J. M., Fryxell, B. A., & Königl, A. 1990, ApJ, 360, 370
Chevalier, R. A. 1984, Ann. NY Acad. Sci., 422, 215
———. 1987, in Proc. ESO Workshop on the SN 1987A, ed. I. J. Danziger (Munich: ESO), 481
———. 1988, Nature, 332, 514
———. 1992a, Nature, 355, 691
———. 1992b, Nature, 355, 617
Chevalier, R. A., & Emmering, R. T. 1989, ApJ, 342, L75
Chevalier, R. A., & Fransson, C. 1987, Nature, 328, 44
Chevalier, R. A., & Imamura, J. N. 1983, ApJ, 270, 554
Chevalier, R. A., & Soker, N. 1989, ApJ, 341, 867
Colella, P., & Woodward, P. R. 1984, J. Comput. Phys., 54, 174
Crotts, A. P. S., & Heathcote, S. R. 1991, Nature, 350, 683
Crotts, A. P. S., Kunkel, W. E., & McCarthy, P. J. 1989, ApJ, 347, L61
Cumming, R. J., & Meikle, W. P. S. 1992, MNRAS, submitted
Dalgarno, A., & McCray, R. A. 1972, ARA&A, 10, 375
Felten, J. E., & Dwek, E. 1991, Proc. ESO/EIPC Workshop, SN 1987A and Other Supernovae, ed. I. J. Danziger & K. Kjär (Garching: ESO), 569
———. 1992, Nature, 356, 202
Fransson, C., Cassatella, A., Gilmozzi, R., Kirshner, R. P., Panagia, N., Sonneborn, G., & Wamsteker, W. 1989, ApJ, 336, 429
Gaetz, T. J., & Salpeter, E. E. 1983, ApJS, 52, 155
Hanuschik, R. W. 1991, A&A, 217, L21
Icke, V., Balick, B., & Frank, A. 1992, A&A, 253, 224
Innes, D. E., Giddings, J. R., & Falle, S. A. E. G. 1987, MNRAS, 226, 67
Jakobsen, P., et al. 1991, ApJ, 369, L63
Livio, M., & Soker, N. 1988, ApJ, 329, 764
Lundqvist, P. 1991, in Proc. ESO/EIPC Workshop, SN 1987A and Other Supernovae, ed. I. J. Danziger & K. Kjär (Garching: ESO), 607
———. 1992, PASP, 104, 787
Lundqvist, P., & Fransson, C. 1991, ApJ, 380, 575
Lundqvist, P., Fransson, C., & Blondin, J. M. 1993, in preparation
Luo, D. 1991, Ph.D. thesis, Univ. Colorado
Luo, D., & McCray, R. 1991, ApJ, 659 (LM)
Mihalas, D. 1978, Stellar Atmospheres (New York: Freeman)
Morris, M. 1981, ApJ, 249, 572
Podsiadlowski, P. 1992, PASP, 104, 717
Podsiadlowski, P., Fabian, A. C., & Stevens, I. R. 1991, Nature, 354, 43
Raymond, J. C. 1979, ApJS, 39, 1
Rousseau, J., Martin, N., Prévot, L., Rebeirot, E., Robin, A., & Brunet, J. P. 1978, A&A, 31, 243
Serlemitsos, P. J., et al. 1992, in Frontiers of X-Ray Astronomy, ed. Y. Tanaka & K. Koyama (Tokyo: Universal Acad.), in press
Shigeyama, T., Nomoto, K., & Hashimoto, M. 1988, A&A, 196, 141
Shull, M., & McKee, C. 1979, ApJ, 227, 131
Staveley-Smith, L., et al. 1992, Nature, 355, 147
Stevens, I. R., Blondin, J. M., & Pollock, A. M. T. 1992, ApJ, 386, 265
Turtle, A. J., et al. 1987, Nature, 327, 38
Underhill, A., & Doazan, V. 1982, B Stars with and without Emission Lines (NASA SP-465)
Vishniac, E. 1983, ApJ, 274, 152
Walborn, N. R., Prévot, M. L., Prévot, L., Wamsteker, W., Gonzalez, R., Gilmozzi, R., & Fitzpatrick, E. L. 1989, A&A, 219, 229
Wampler, E. J., Wang, L., Baade, D., Banse, K., D'Odorico, S., Gouiffes, C., & Tarenghi, M. 1990, ApJ, 362, L13
Wang, L. 1991, A&A, 246, L69
Wang, L., & Mazzali, P. A. 1992, Nature, 355, 58 (WM)
Weiler, K. W., Sramek, R. A., Panagia, N., van der Hulst, J. M., & Salvati, M. 1986, ApJ, 301, 790
White, G. L., Argue, A. N., & Van Leeuwen, F. 1992, Nature, submitted
Woodward, P. R., & Colella, P. 1984, J. Comput. Phys., 54, 115
Woosley, S. E. 1988, ApJ, 330, 218
Zuckerman, B. 1980, ARA&A, 18, 263